ECCENTRIC ORBITS AROUND PLANETARY MOONS*

Ryan P. Russell† and Adam T. Brinckerhoff ‡

Eccentric orbits in the third-body perturbed problem are evaluated in the context of planetary moon missions. All possible motion in the doubly averaged problem is overviewed and concisely summarized via contour plots. Special attention is paid to the well known class of orbits that cycle between low and high eccentricity while circulating in argument of periapse. Applying the doubly averaged assumptions, the maximum sustainable inclinations and eccentricities for long-term, circulating, ballistic orbits are found and discussed for the dimensioned systems at Ganymede, Europa, Titan, Enceladus, and several other planetary moons. The full cycle periods of the circulations and librations are reduced to quadratures that are functions only of the two integrals of motion and the moon and orbiter mean motions. In the specific case of Ganymede, higher fidelity models are considered to analyze the validity of the doubly averaged assumptions. Families of stable, long-repeat cycle, periodic orbits are demonstrated in the un-averaged Hill plus non-spherical potential model. Several point designs are considered in a full ephemeris model, and promising results include long-term ephemeris stable orbits that enjoy maximum inclinations above 60 degrees. These circulating "ball-of-yarn" orbits cycle between high and low eccentricities while distributing close approaches throughout all longitudes. Further, these largely non-Keplerian orbits are less expensive to achieve than low-altitude, circular orbits, and the orbital geometry and timing are favorable for a variety of both planetary moon and system science.

NOMENCLATURE

Symbol	***Description***
$a, e, i, \omega, \Omega, \upsilon$	Classical orbital elements: semi-major axis, eccentricity, inclination, argument of periapse, longitude of ascending node, true anomaly
alt	Altitude
a_s	Moon semi-major axis
b_1 , b_2	Stability indices
C	Jacobi integral of motion
C_1 , C_2	Integrals of motion in the doubly averaged system
$C_{n,m}$, $S_{n,m}$	n^{th} degree and m^{th} order non-zonal gravity field coefficients
J_n	n^{th} degree zonal gravity field coefficient
n	Spacecraft mean motion
N_s	Moon mean motion
r	Radius magnitude of the spacecraft position
R	Moon radius
r_p	Spacecraft periapse
t	Time
T	Spacecraft period
T_c	Full contour cycle period
T_s	Moon period
U	Non-spherical gravity potential
x, y, z, u, v, w	Rotating, body-fixed state components
Γ	Potential function
ε	Small number
μ_p	Planet gravitational parameter
μ_s	Moon gravitational parameter

* Presented as Paper AAS 08-181 at the AAS/AIAA Space Flight Mechanics Meeting in Galveston, TX, Jan. 2008.

† *Currently*: Assistant Professor, Guggenheim School of Aerospace Engineering, Georgia Institute of Technology, 270 Ferst Drive, Atlanta, GA, 30332-0150, 404-385-3342, ryan.russell@gatech.edu; *Formerly*: Jet Propulsion Laboratory, 4800 Oak Grove Drive, Pasadena, California 91109.

‡ Graduate student, Guggenheim School of Aerospace Engineering, Georgia Institute of Technology, adam.brinckerhoff@gatech.edu

INTRODUCTION

The topic of science orbit design around planetary moons is broad and has been the subject of many studies in recent years. See, for example, Refs. [1-19]. In order to ensure global coverage, adequate surface mapping, and tidal bulge detection, science orbits are generally required to have high-inclination, low-altitude, and low-eccentricity. Unfortunately, it is well known that most orbits about planetary satellites with these properties will eventually impact due to dynamic instability from the third-body perturbation. While low altitude, near-polar orbits are unstable and expensive to achieve in many cases, eccentric high-altitude orbits have received much less attention in terms of mission design applications. One recent application involves constellation design at the Earth's moon [18] noting that the averaged third-body dynamics predict the existence of mid-inclination stable eccentric frozen orbits. A second class of orbits predicted by the averaged third-body dynamics [2] and further demonstrated as periodic orbits in the un-averaged third-body problem [13,14] are the circulating and librating orbits that indefinitely cycle between various degrees of high and low eccentricities. While these orbits have been observed and documented in the normalized Hill's problem and a few dimensioned cases such as Europa, their general mission design application has yet to be fully explored. In this study we review all types of motion predicted in the doubly averaged third-body problem with particular emphasis on eccentric orbits, regions of validity for doubly averaged motion, and implications of the different time and distance scales associated with planetary moons of interest. In particular, we choose Ganymede as a promising application for these circulating eccentric orbits and several examples are demonstrated. The doubly-averaged assumptions are verified with the identification of periodic orbits in the un-averaged model [14], and the preliminary robustness of the orbit designs to realistic force perturbations is verified with ephemeris propagations.

While the low-altitude near-circular orbits are quite sensitive to non-spherical gravity, the inclusion of higher order terms is found to be a second order effect for the high-altitude eccentric orbits. The largely analytical averaging techniques from [2] only include point mass effects of the bodies and [4,9,10] consider a few dominant non-spherical terms especially in the case of the circular orbits. While the inclusion of the higher order terms may prove difficult using averaging techniques, including at least the dominant terms for detailed eccentric orbit applications is considered future work. The periodic orbit approach implemented in this study is amenable to including these higher order terms, even in the case of a highly irregular shaped body [14]. The rapid identification of the periodic orbits in a full gravity field is well suited for future Monte-Carlo analyses that will certainly be required to investigate gravity field sensitivities.

MODELS OVERVIEW

The classic restricted three body model assumes that the moon and planet are point masses and that they orbit their common center with a constant radius. The Hill's model is the limiting case where the moon to planet mass ratio approaches zero[†]. This assumption results in a tidal force field that is symmetric about the plane passing through the moon center and perpendicular to the planet moon line [2]. The Hill's model becomes more valid as the mass ratio and spacecraft to moon distance decrease. By using Hill's model, the normalized equations of motion remain unchanged for all planetary moon systems, and the dimensioned states for specific moon systems are found simply through the un-normalization process.

The dynamical model for the Hill problem superimposed by an n x n spherical harmonic moon gravity field is depicted in Figure 1. Given the additional assumption that the rotation of the moon is synchronous with its orbital period, the moon-fixed reference frame is identical to the moon-centered rotating Hill's frame. Periodic orbits in this model represent dynamic equilibria in the un-averaged equations, and they are relied upon in this study to verify stability and motion predictions from the simplified doubly averaged system.

[†] formally, the Hill approximation requires $(\mu_s/\mu_p)^{1/3} << 1$

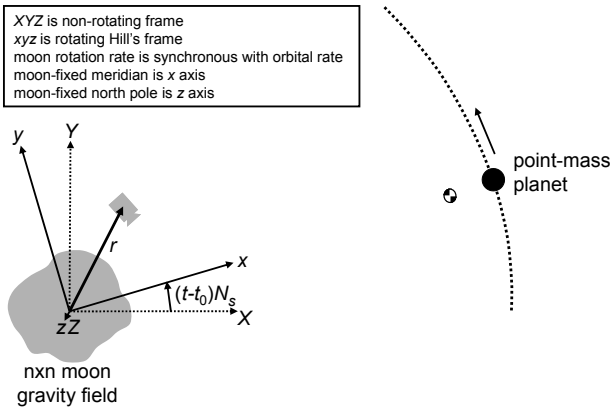

Figure 1: Hill's model plus nxn potential model

Table 1 gives the dimensioned parameters and associated normalized Hill's model units for a specific application at Ganymede. For cases including non-spherical Ganymede gravity terms, the Appendix includes a representative 4x4 Ganymede gravity field. The J_2 and C_{22} terms were estimated with reasonable confidence based on Galileo flyby data, while the remaining terms are simply representative of an expected field.

Table 1: Jupiter-Ganymede system parameters

Parameter	Value
Ganymede gravitational parameter	9886.99742842995 km^3/s^2
Jupiter gravitational parameter	1.26618626797685e8 km^3/s^2
Jupiter - Ganymede distance	1.0704e6 km
Ganymede mean radius	2631.2 km
Hill's normalized time unit (derived)	98413.2095723724 s
Hill's normalized length unit (derived)	45749.9268762215 km
System mean motion (derived)	1.016123754468760e-5 rad/s

The equations of motion for the Hill's plus full gravity model (see Figure 1) are given in Eq. (1).

$$\begin{aligned} \ddot{x} &= 2N_s v + \partial\Gamma/\partial x \\ \ddot{y} &= -2N_s u + \partial\Gamma/\partial y \\ \ddot{z} &= \partial\Gamma/\partial z \end{aligned} \tag{1}$$

The potential function, Γ, is introduced in Eq. (2) where U is the contribution due to the non-spherical moon, and it is expressed via the standard spherical harmonic expansion [20]. Typically, canonical units (LU and TU) are derived based on normalizing the moon mean motion, N_s, to unity.

$$\begin{aligned} \Gamma &= \frac{1}{2} N_S{}^2 \left(3x^2 - z^2\right) + \mu/r + U \\ r &= \sqrt{x^2 + y^2 + z^2} \end{aligned} \tag{2}$$

The system is Hamiltonian and admits C, an integral of motion given in Eq. (3) that is analogous to the Jacobi constant.

$$C = 2\Gamma - \left(u^2 + v^2 + w^2\right) \tag{3}$$

In the case of a point mass moon, a reduction of the system leads to the doubly averaged model where the Hill's model potential is averaged twice: once over one spacecraft orbit and once over one moon orbit. The basic averaging assumption is that the spacecraft period is much smaller than the moon period. Typically an order of magnitude difference in these periods justifies the use of the averaging approximation [10]. In the current study,

we examine a range of system to spacecraft period ratios, evaluate the validity of the underlying averaging assumptions, and interpret the implications of this ratio to the broader context of mission design. When the equations of motion from Eq. (1) are formulated using the partial derivatives of the potential and Lagrange's planetary equations [2,10,21], the doubly averaged system leads to Eqs. (4)-(8).

$$\frac{da}{dt} = 0 \tag{4}$$

$$\frac{de}{dt} = \frac{15}{8}\frac{N_S^2}{n} e\sqrt{1-e^2}\sin^2 i \sin 2\omega \tag{5}$$

$$\frac{di}{dt} = -\frac{15}{16}\frac{N_S^2}{n}\frac{e^2}{\sqrt{1-e^2}}\sin 2i \sin 2\omega \tag{6}$$

$$\frac{d\omega}{dt} = \frac{3}{8}\frac{N_S^2}{n}\frac{1}{\sqrt{1-e^2}}[5\cos^2 i - 1 + 5\sin^2 i \cos 2\omega + e^2(1-5\cos 2\omega)] \tag{7}$$

$$\frac{d\Omega}{dt} = -\frac{3}{8}\frac{N_S^2}{n}\frac{\cos i}{\sqrt{1-e^2}}(2 + 3e^2 - 5e^2\cos 2\omega) \tag{8}$$

Selected ephemeris propagations are carried out to demonstrate the robustness of simplified model solutions to perturbations associated with realistic force models. The ephemeris states of the planets, moons, and the Sun are based on publicly available data from the Jet Propulsion Laboratory*. The body poles and prime meridians are based on the most recent data from the IAU Working Group on Cartographic Coordinates and Rotational Elements of the Planets and Satellites [22].

DOUBLY AVERAGED THIRD-BODY SYSTEM

The first order dynamics of orbiters in the vicinity of point-mass planetary moon orbiters are captured nicely through averaging techniques that reduce the problem's dimension from six to three, enabling a thorough characterization of possible motion. For details on studies that rely on averaging see for example [2,4,9,10,23,24].

From Eqs. (4)-(8), note that semi-major axis is constant and the evolutions of eccentricity, inclination, and argument of periapse do not depend on longitude of the ascending node. Therefore, the basic characteristics of the orbit are practically reduced to the three variables e, i, and ω. Further, Broucke [2] shows that the reduced system includes two constant integrals of motion shown in Eqs. (9) and (10).

$$C_1 = \left(1-e^2\right)\cos^2 i \tag{9}$$

$$C_2 = e^2\left(2/5 - \sin^2 i \sin^2 \omega\right) \tag{10}$$

Therefore, given an initial state for e, i, and ω, the system is reduced to one degree of freedom as it is confined to remain on constant contours of C_1 and C_2. Figure 2 captures all types of motion allowed based on the feasible values of C_1 and C_2. The x-axis on each of the plots is $e\cos\omega$ and the y-axis is $e\sin\omega$. Therefore, the plot can be thought of in polar coordinates where the eccentricity magnitude is the radius coordinate and the argument of periapse is the angle. Each picture shows a constant value of C_1 as indicated in the title. Note that C_1 can take on any value in the range from zero to one, and the C_2 range depends directly on C_1 (see [2] for details about the feasible regions of the C_1-C_2 plane). Contours of constant C_2 values are illustrated on each sub-plot. The figure-eight shaped contour in each plot reflects a C_2 of approximately zero ($\varepsilon > 0$) while the remaining contours are distributed among feasible values based on the given C_1.

*URL: http://naif.jpl.nasa.gov/naif/spiceconcept.html [cited 21 Jun 2006].
URL: ftp://naif.jpl.nasa.gov/pub/naif/generic_kernels/spk/planets/de414.bsp [cited 21 Jun 2006].
URL: ftp://naif.jpl.nasa.gov/pub/naif/generic_kernels/spk/satellites/jup230.bsp [cited 21 Jun 2006].
URL: ftp://naif.jpl.nasa.gov/pub/naif/generic_kernels/pck/pck00008.tpc [cited 21 Jun 2006].

If a spacecraft is initiated with a particular C_1 and C_2, then its motion is limited to the corresponding contour line as long as no thrusting occurs. The rate at which the spacecraft moves around the contour line is influenced by a; however, the shape of the contour lines are independent of a. Inclination is indicated by different shades and is independent of the contour lines. Inverse of eccentricity, inclination finds its maximum at the center of each plot and its minimum (0°) along the outer circumference. Thus, as the system moves along the constant C_2 lines, e, i, and ω change accordingly. Note that eccentricities ranging from zero to one are feasible in the limit as C_1 approaches zero, while only $e = 0$ is valid in the limit as C_1 approaches one.

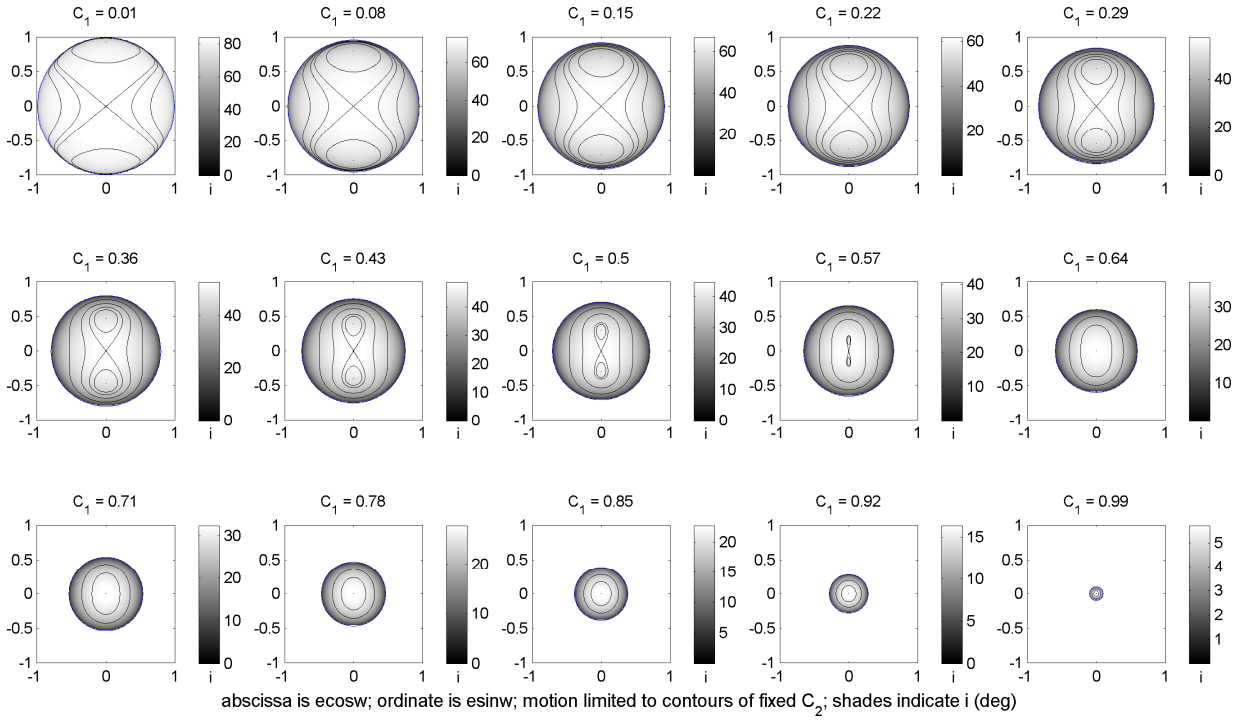

Figure 2: Overview of possible orbital motion in the doubly averaged system

The motion illustrated in Figure 2 is characterized by two basic features. When $C_1 > 3/5$, all contour lines circulate around the center of the plot; therefore, argument of periapse circulates. The shape of the contours is circular towards the center and the boundary of each plot, while the interior regions find vertically elongated contours indicating the eccentricity will grow and shrink during each pass around the contour. Following a bifurcation at $C_1 = 3/5$, two islands emerge and move away from the center as C_1 decreases. Figure 3 shows this specific range of motion in a similar fashion to Figure 2, with the addition of the normalized full cycle contour period, T_c, to be discussed later. Here, the motion is restricted to either librate around one of the islands or circulate around both islands. At the center of each island a frozen orbit exists that is stable because the neighboring orbits simply librate with near-constant eccentricity and argument of periapse. The two frozen orbits are represented on each plot by contours that appear as small dots above and below the origin, and the ovular contours around them represent possible librating orbits. For circulating orbits when $C_1 < 3/5$, note that the maximum inclination occurs when e ~ 0 and each cycle around the contour leads to maximum eccentricity at the top and bottom of each plot (corresponding to $\omega = \pm 90°$). For $e = 0$, the emergence of the islands (the bifurcation at $C_1 = 3/5$) corresponds to a stability boundary of $i \sim 39°$. Thus, all initially circular orbits with $i > 39°$ will repeatedly grow and shrink in e as the contours require either a librating or circulating cycle around one or both islands, respectively.

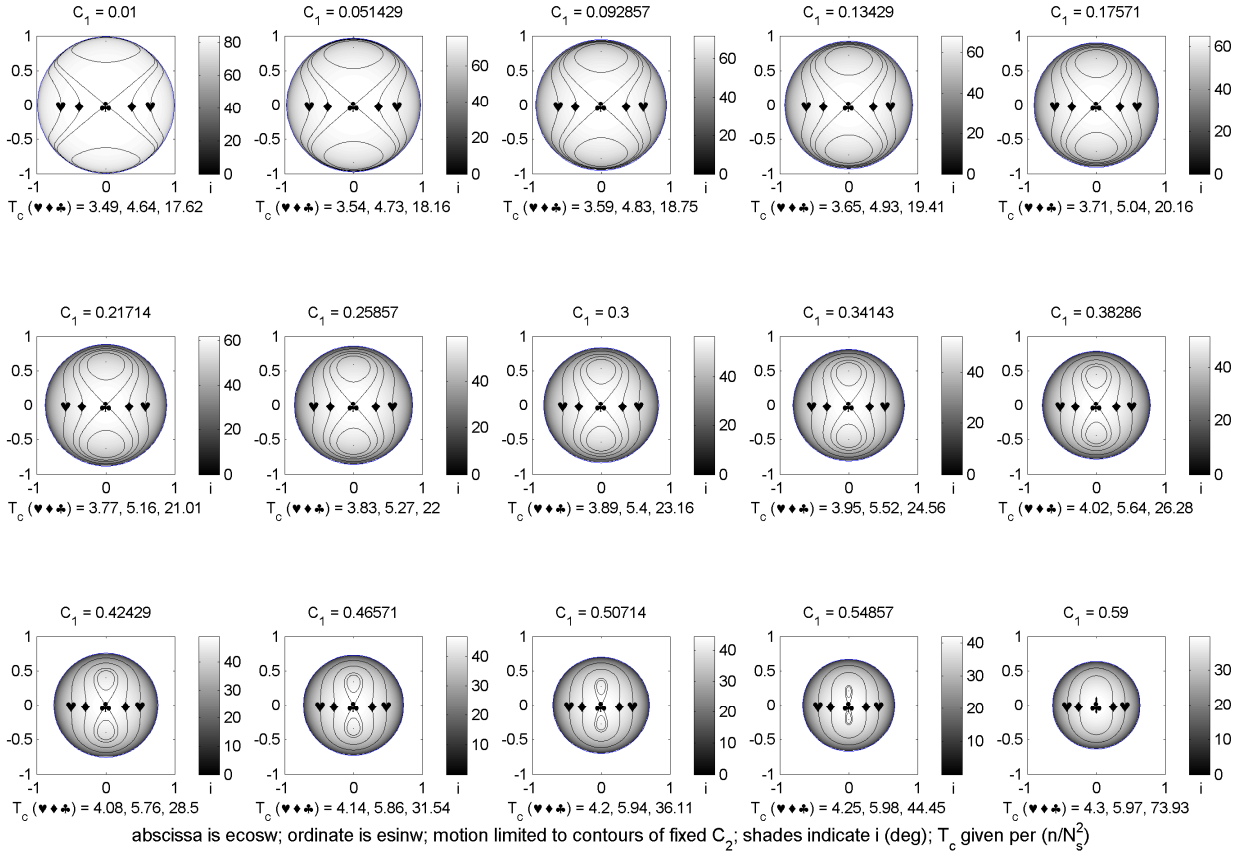

Figure 3: Overview of post-bifurcation motion in the doubly averaged system

As an example, if a spacecraft starts with (e_0, i_0, ω_0) = (0.001, 56.8°, 0°), then $C_1 \sim 0.3$. Figure 4 shows that the resulting contour (♣) circulates around both islands, and e and i range from ~0 to ~0.7 and ~39° to ~56.8° respectively. This type of circulating orbit is termed a "figure eight" orbit due to its contour's shape. Note that it achieves the highest possible inclination of all the circulating orbits and has a C_2 of slightly above zero by definition. For practical consideration, the figure-eight orbits are attractive to the science community because (1) their circulating nature distributes close approaches through different latitudes and longitudes, (2) they enjoy the maximum possible inclinations of all the circulating orbits, (3) their long periods and high altitudes enable unique opportunities for planet system science, and (4) they cost less to achieve in comparison to traditional low-altitude circular orbits.

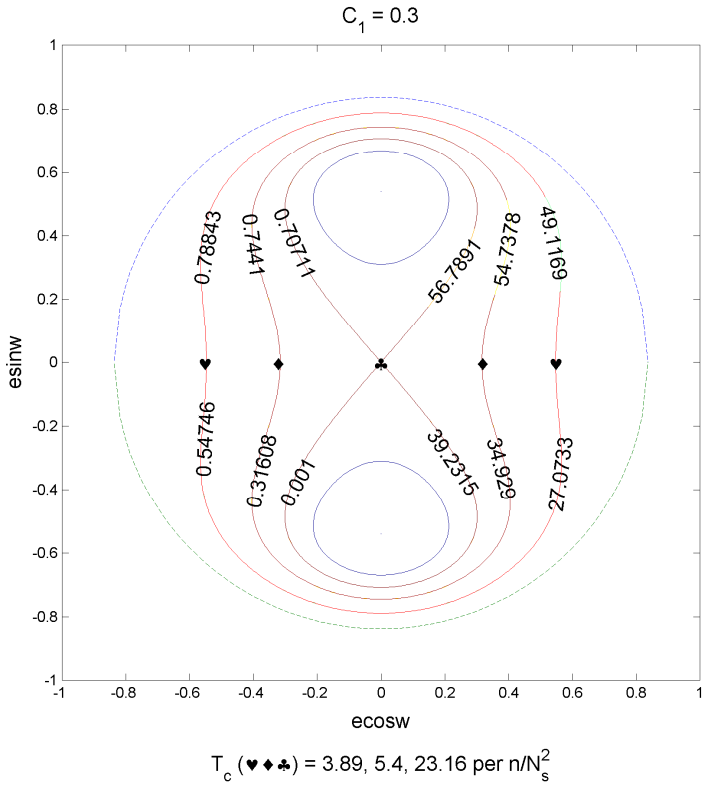

T_c (♥♦♣) = 3.89, 5.4, 23.16 per n/N_s^2

dotted: e boundary; left: contour e range; right: contour i range (deg); motion limited to contours of fixed C_2

Figure 4: Sample post-bifurcation motion in doubly averaged third body problem

If the initial conditions are the same as above except $\omega_0 = 90°$, the contour librates around just the top island with a very similar range in i and e. In terms of mission design, a circulating trajectory will find close approach locations distributed amongst different latitudes, while a librating trajectory will find the close approach locations centered near the orbit inclination latitudes on either the northern or southern hemisphere. As seen in Figure 3 and Figure 4, each circulating contour has an associated full cycle period, which is defined as the amount of time necessary for the spacecraft to complete one trip around its constant C_2 curve. A circulating orbit's full cycle period can be calculated by numerical integration of Eqs. (5)-(7) or more simply from the quadrature given in Eq. (11) using the bounds from Eqs. (12) and (13).

$$T_c = \frac{16}{3}\frac{n}{N_s{}^2}\int_{e_0}^{e_f} \frac{e\sqrt{1-e^2}}{\sqrt{\left(2e^2-5C_2\right)\left(e^2-1\right)\left[3e^4+(5C_1+5C_2-3)e^2-5C_2\right]}}de \tag{11}$$

$$e_0 = \sqrt{C_2 5/2} \tag{12}$$

$$e_f = \frac{1}{6}\sqrt{6\sqrt{25(C_1{}^2+C_2{}^2+2C_1C_2)+30(C_2-C_1)+9}-30(C_1+C_2)+18} \tag{13}$$

The quadrature for the full cycle contour period is derived from Eq. (5) by separating variables, expressing i and ω in terms of e, C_1 , and C_2 using Eqs. (9) and (10), simplifying, and integrating both sides. Each circulating contour is symmetric about both the x and y axes; therefore, the eccentricity bounds are found using Eqs. (9) and (10) at $\omega = 0°$ and $\omega = 90°$, and the T_c expression is accordingly quadrupled. An expression for the full cycle contour period of a librating orbit can be found using a similar procedure; where in this case, the eccentricity bounds in Eqs. (14) and (13) are found using the two positive roots of the resulting quartic at $\omega = 90°$. Further, the T_c expression in the librating case is doubled instead of quadrupled because its contour is symmetric only about the

y axis, which results in a constant coefficient of 8/3 instead of 16/3 in Eq. (11). Note that the periods provided in Figure 3 and Figure 4 are expressed as non-dimensioned factors of n/N_s^2, where, in general, the full cycle period is only a function of n, N_s, C_1, and C_2. The full cycle period finds its maximum dimensionless value at $C_2 \sim 0$, and the quick and non-linear reduction in period as a function of initial eccentricity (at $\omega_0 = 0°$) is clearly apparent when viewing the cycle period labels in Figure 3.

$$e_0 = \frac{1}{6}\sqrt{-6\sqrt{25\left(C_1^2 + C_2^2 + 2C_1C_2\right) + 30\left(C_2 - C_1\right) + 9} - 30\left(C_1 + C_2\right) + 18} \tag{14}$$

Note that each of the eccentricity limits shown in Eqs. (12)-(14) causes the denominator of the integrand of Eq. (11) to equal zero, which makes the integral in this equation singular. For practical purposes, the numerical integration of this equation should be performed slightly within the appropriate bounds to avoid these singularities; this method produced very accurate full cycle period values when compared to corresponding numbers taken from a numerical propagation of Eqs. (5)-(7). Also, C_1 and C_2 should not be exactly 3/5 and zero, respectively, in order to avoid numerical singularities associated with the bifurcation between circulating and librating orbits.

Based on the premise that the science community prefers high inclinations for favorable mapping and observation purposes, we note in Figure 3 that the upper bound of inclination on a figure-eight orbit (occurring at $e = 0$) increases for smaller C_1 values. The corresponding upper bound on eccentricity (occurring at $\omega = \pm 90^o$) also increases for smaller C_1. Therefore, in order to maximize inclination for a figure-eight orbit around a specific planetary moon, we select a C_1 value such that the upper bound on the eccentricity cycle leads to an orbit with a grazing periapse altitude and an apoapse altitude reaching to the furthest limits of the doubly averaged model validity. The minimum periapse radius is based on the sum of the moon's radius and an assumed 100 km minimum altitude, while the maximum apoapse is based on the largest possible radius orbit that remains valid in the doubly averaged model. Equations (15) and (16) express the resulting maximum a and e derived from simple two-body geometry.

$$a_{\max} = a_s\left[\frac{\mu_p}{\mu_s}\left(\frac{T_s}{T}\right)^2\right]^{-1/3} \tag{15}$$

$$e_{\max} = 1 - \frac{(R + alt_{\min})}{a_{\max}} \tag{16}$$

Noting that C_1 is constant, the right hand side of Eq. (9) applied at $\omega = 0°$ (where $e = 0$ and $i \sim i_{\max}$) can be equated to the same expression applied at $\omega = 90°$ (where $e = e_{\max}$ and $i \sim 39°$). The result is simplified to produce the maximum inclination relationship given in Eq. (17).

$$i_{\max} = \arccos\sqrt{\left(1 - e_{\max}^2\right)3/5} \tag{17}$$

Therefore, the figure-eight orbit will oscillate between inclinations of ~39° and $i_{\max}$. A figure-eight orbit's C_2 value is always slightly above zero, but C_1 is dependent on the physical parameters of the system and orbiter. Because the maximum inclination occurs at zero eccentricity, Eq. (9) easily reduces to Eq. (18).

$$C_1 = \cos^2 i_{\max} \tag{18}$$

Thus, figure-eight orbit full cycle contour period values for each moon system can be found using Eqs. (11)-(13), (16), (17), and (18) accordingly. Table 2 shows these parameters for several different moon systems in our solar system. Note that the list of systems is taken from [10] where characteristic instability times are presented for low altitude circular orbits of potential moons of interest. The data in the first seven columns of Table 2 comes from the physical parameters of each system as well as basic orbital mechanics equations, and the data in the last three columns comes directly from the equations of the doubly averaged third-body system. Note that the data given in Table 2 is based on figure-eight orbits with very small but non-zero initial e, while a realistic trajectory would likely start with a greater eccentricity to avoid the bifurcation to a librating orbit. As mentioned previously and appreciated in Figure 3, the circulating orbits with larger initial e (for example, 0.1) will find from Eq. (11) significantly shorter full cycle periods than those reported in Table 2.

Table 2: Figure-eight science orbits with maximum inclinations[b] for different moon systems

Satellite	μ_s (km^3/s^2)	r_p [a] (km)	a_s (km)	T_s (days)	a_{max} [b] (km)	e_{max} [b]	C_1 [b]	i_{max} [b] (deg)	T_c [b] (days)
Earth (μ_p=398479.14 km^3/s^2)									
Moon	4902.801	1838	384400	27.46	19119	0.904	0.110	70.6	832.7
Mars (μ_p=42815.397 km^3/s^2)									
Phobos	0.0007158	111	9380	0.32	5	-20.500	-251.57	N/A	N/A
Deimos	0.000098	106	23460	1.26	7	-14.944	-133.39	N/A	N/A
Jupiter (μ_p=126649960 km^3/s^2)									
Io	5959.916	1922	421800	1.77	3281	0.414	0.497	45.2	98.0
Europa	3202.739	1661	671100	3.55	4244	0.609	0.378	52.1	147.4
Ganymede	9887.834	2731	1070400	7.16	9856	0.723	0.286	57.6	259.6
Callisto	7179.289	2510	1882700	16.69	15581	0.839	0.178	65.1	537.8
Amalthea	0.138	183	181400	0.50	40	-3.562	-7.011	N/A	N/A
Thebe	0.1	149	221900	0.68	44	-2.379	-2.795	N/A	N/A
Adrastea	0.0005	108	129000	0.30	4	-23.633	-334.52	N/A	N/A
Metis	0.008	122	128000	0.30	11	-10.063	-60.160	N/A	N/A
Saturn (μ_p=37918950 km^3/s^2)									
Mimas	2.53	299	185540	0.94	162	-0.843	0.174	N/A	N/A
Enceladus	7.21	352	238040	1.37	295	-0.195	0.577	N/A	N/A
Tethys	41.21	636	294670	1.89	653	0.025	0.600	39.3	193.9
Dione	73.113	663	377420	2.74	1012	0.345	0.528	43.4	172.6
Rhea	154.07	865	527070	4.52	1812	0.523	0.436	48.7	210.6
Titan	8978.19	2676	1221870	15.95	16286	0.836	0.181	64.8	515.4
Hyperion	0.37	233	1500880	21.71	691	0.663	0.336	54.5	843.4
Uranus (μ_p=398479.14 km^3/s^2)									
Ariel	90.3	679	190900	2.52	1028	0.340	0.531	43.2	160.9
Umbriel	78.2	685	266000	4.15	1366	0.499	0.451	47.8	200.4
Titania	235.3	889	436300	8.72	3234	0.725	0.285	57.8	315.5
Oberon	201.1	861	583500	13.48	4104	0.790	0.225	61.7	455.8
Miranda	4.4	336	129900	1.42	256	-0.314	0.541	N/A	N/A
Neptune (μ_p=398479.14 km^3/s^2)									
Triton	1427.9	1453	354800	5.87	4531	0.679	0.323	55.4	223.7
Pluto (μ_p=398479.14 km^3/s^2)									
Charon	108	693	17536	5.70	1880	0.631	0.361	53.1	230.1

[a] $r_p = r + alt_{\min}$, $alt_{\min}$ = 100 km
[b] $T_s/T = 10$

From Table 2, five of the figure-eight science orbit parameters for each moon system directly depend on the ratio between moon period and spacecraft period (T_{sys}/T). Clearly, the maximum sustainable inclinations for a particular moon system are directly related to the relative size of the third body perturbation. In general (and as expected), the maximum sustainable inclinations increase for larger moons and moons further from their associated planet. The values presented in Table 2 are based on an order of magnitude period ratio, which was stated before as the necessary value to justify the averaging approximation. Negative maximum eccentricities in the table above correspond to moon systems that have no possible figure-eight science orbits at this particular period ratio. As the magnitude of period ratio is decreased, maximum eccentricity and maximum inclination change accordingly. The specific trends of this change for the four outer planet flagship moons[*] (Europa, Ganymede, Enceladus, and Titan) are shown in Figure 5.

[*] http://www.lpi.usra.edu/opag/announcements.html [cited Dec 19 2007]

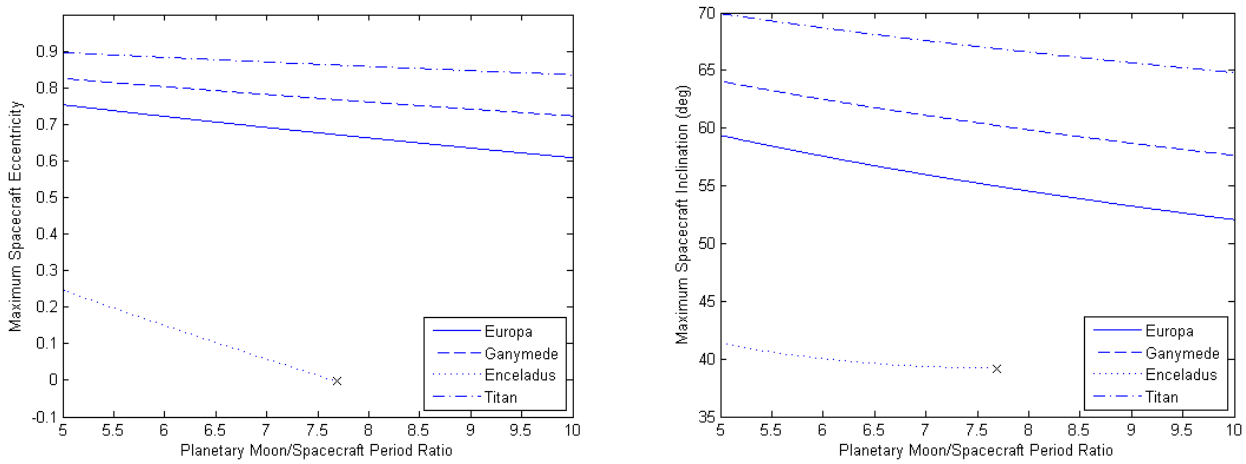

Figure 5: Maximum inclination and eccentricity as a function of the model-justifying period ratio

The figure-eight orbit maximum eccentricities and inclinations increase as the justifying period ratio decreases. The nominal order of magnitude period ratio is an estimate for a justified averaging approximation [10]. Note that the period ratio boundary between valid and invalid use of averaging is debatable and it varies for each different moon system and application. Figure 5 shows that a figure-eight orbit is possible for Enceladus[†] at a period ratio of five, but the spacecraft would violate the minimum altitude constraint at any ratio above ~7.7. Alternatively, Ganymede, Europa, and Titan enjoy figure-eight orbits with large eccentricities across the entire period ratio range shown. Previous work that documents families of periodic orbits around planetary moons [25,26] indicate that perturbed Keplerian orbits either cease to exist or find dramatic character changes much beyond roughly 2/5 of the Lagrange point distance, which corresponds to a period ratio of ~7. Numerical simulations verify that the doubly averaged predictions match closely the full dynamics when the period ratio is at or above ~10. For larger values, the doubly averaged predictions degrade in accuracy.

Considering Ganymede as an example, Table 2 shows that the doubly averaged system is well suited for predicting motion when the semi-major axis is less than or equal to ~9,856 km. At this semi-major axis length, a 100 km minimum altitude orbiter at Ganymede can sustain rather large eccentricities (up to ~0.723) without impacting. Further, the large altitudes reduce the sensitivity to non-spherical gravity. Therefore, Ganymede is an excellent application for the doubly averaged circulating and librating trajectories that often lead to large eccentricity excursions. Accordingly, we design a highly inclined 24-hour eccentric orbit at Ganymede (a reference orbit for the Jupiter System Observer flagship study from FY07). The 24 hour period requires an average semi-major axis of ~12,320 km. While this exceeds the just mentioned formal limit of ~9,856 km, we proceed in order to test the period ratio limit of applicability for the doubly averaged system at this particular moon. The 24-hour period is synchronous with typical work shifts and is therefore highly desirable in terms of staffing and operations. An orbit is sought with distributed low-altitude close approaches and high inclinations for favorable science geometry. The fourth subplot from the left in the first row of Figure 2 shows a figure-eight contour with $C_1 = 0.22$ yielding an oscillating orbit eccentricity that varies between near circular and ~0.78 with a maximum inclination of ~61°. This circulating 24 hour orbit leads to a 925 x 19,650 km altitude orbit. In the following section, we seek to verify the averaging assumptions by identifying and comparing periodic orbits in the un-averaged model with similar orbital element evolutions.

[†] Note that Ref. [19] documents stable circulating science orbits at Enceladus with inclinations as high as 65°. However, these orbits exist well into the region where the doubly averaged model fails to predict the un-averaged motion.

THE UN-AVERAGED MODEL

A second general technique for analyzing motion near planetary moons involves the search and characterization of periodic orbits in un-averaged models. See [4,5,6,11,12,13,14,16,17] for details. The periodic orbits are crucial for characterizing the motion in instances when the doubly averaged assumptions are not valid [4,5,12,13]. In cases inside the region of validity, the periodic orbits provide higher order solutions.

The local periodic orbit search is performed in Hill's model superimposed on an n x n spherical harmonic gravity field. The Hill's potential and non-spherical two-body potential are both time invariant; therefore, an abundance of periodic orbits exists and computational searches are relatively fast. A general use prototype software package called *Groove*[‡] is used to find and analyze periodic orbits and families of orbits. The algorithms and concepts are explained and demonstrated in [6,11,14].

Starting with the initial conditions $\{a_0 = 12{,}320$ km, $i_0 = 60^o$, $e_0 = 0.1$, $\omega_0 = \Omega_0 = \upsilon_0 = 0^o\}$, the un-averaged equations (including the non-spherical terms) are propagated until a full circulation in the $e\ \omega$ plane completes. For this example it requires approximately 81 revolutions. We therefore seek a periodic orbit that closes in the body fixed frame after 81 revolutions. The ~80 day period is consistent with 70.3 day period calculated using the quadrature from Eq. (11). The differential corrector converges to the initial conditions given in Table 3.

Table 3. Example periodic orbits in Hill's model plus 4x4 Ganymede gravity field*

Property	Units	12:81 unstable orbit	9:56 stable orbit
x_0	km	-1.10294724E+04	1.27215637E+04
y_0	km	6.09916977E+02	2.74572065E+03
z_0	km	-9.92043402E-15	0.00000000E+00
u_0	km/s	-2.56020704E-02	-5.19574390E-01
v_0	km/s	-4.71573204E-01	3.16290562E-01
w_0	km/s	8.73907974E-01	6.25411458E-01
a_0	km	1.23072793E+04	1.30393130E+04
e_0	-	1.02457203E-01	5.05659039E-01
i_0	deg	6.16128288E+01	5.61929409E+01
ω_0	deg	2.94588490E-01	1.20188898E+02
Ω_0	deg	1.76834834E+02	1.21794367E+01
υ_0	deg	-2.94588490E-01	-1.20188898E+02
T_c	day	7.75866851E+01	5.70386714E+01
avg. i	deg	56.18	56.22

*Initial conditions given in non-rotating frame aligned with the IAU defined Ganymede body-fixed frame at epoch.

The natural family of similar orbits is then found by targeting neighboring Jacobi constant values. The effect of changing the Jacobi constant on this family in the vicinity of the orbit of interest is small changes in average inclination. Figure 6 shows the family of orbits as a function of average inclination. The 12:81 family indicates that the spacecraft makes 81 revolutions while Ganymede makes $12+\Delta\Omega$ revolutions prior to closing the periodic orbit in the body fixed frame. The ratio of the two integers can be adjusted in order to change the average semi-major axis [14].

The stability indices b_1 and b_2 from Figure 6 must both be less than or equal to two for linear stability. Most of the orbits of Figure 6 are therefore mildly unstable indicating that the exact repeat ground tracks will eventually be destroyed when propagated for long periods. The implications of the instability will be further investigated with ephemeris propagations in a later section. The stated periodicity is a measure of how closely the targeted final state matches the initial state, and 10^{-q} is roughly equivalent to matching q significant digits.

‡ The Groove software package (developed primarily at the Jet Propulsion Laboratory, written in Fortran 90, and available on linux and PC platforms) represents a new capability for the rapid design of science orbits and can benefit missions desiring global surface coverage, maximum orbital stability, predictable orbital elements, sun-synchronicity, and/or high-fidelity repeat ground tracks. Example applications include but are not limited to: Europa, Ganymede, Enceladus, Vesta, the Moon, Earth, and Mars.

To demonstrate the properties of a particular orbit, Figure 7 - Figure 9 show characteristics of an example 12:81 periodic orbit propagated for one period. The three-body nature of the orbit is appreciated in the large variations seen in the osculating orbital elements shown in Figure 7. The orbit has altitudes ranging from ~1000-18500 km, eccentricities ranging from 0.02 to 0.7, and inclinations ranging from 45^{o} to 62^{o}. The argument of periapse is clearly of the circulating nature as it cycles exactly once in the ~78 day period. The quickly processing and librating orbits are appropriately coined "ball-of-yarn" orbits as the body-fixed trajectory plot in Figure 7 illustrates. The repeat ground tracks and the associated close approach locations are illustrated in Figure 8. The figure-eight path of the eccentricity vector in Figure 9 clearly resembles the circulating contours predicted from the doubly averaged system.

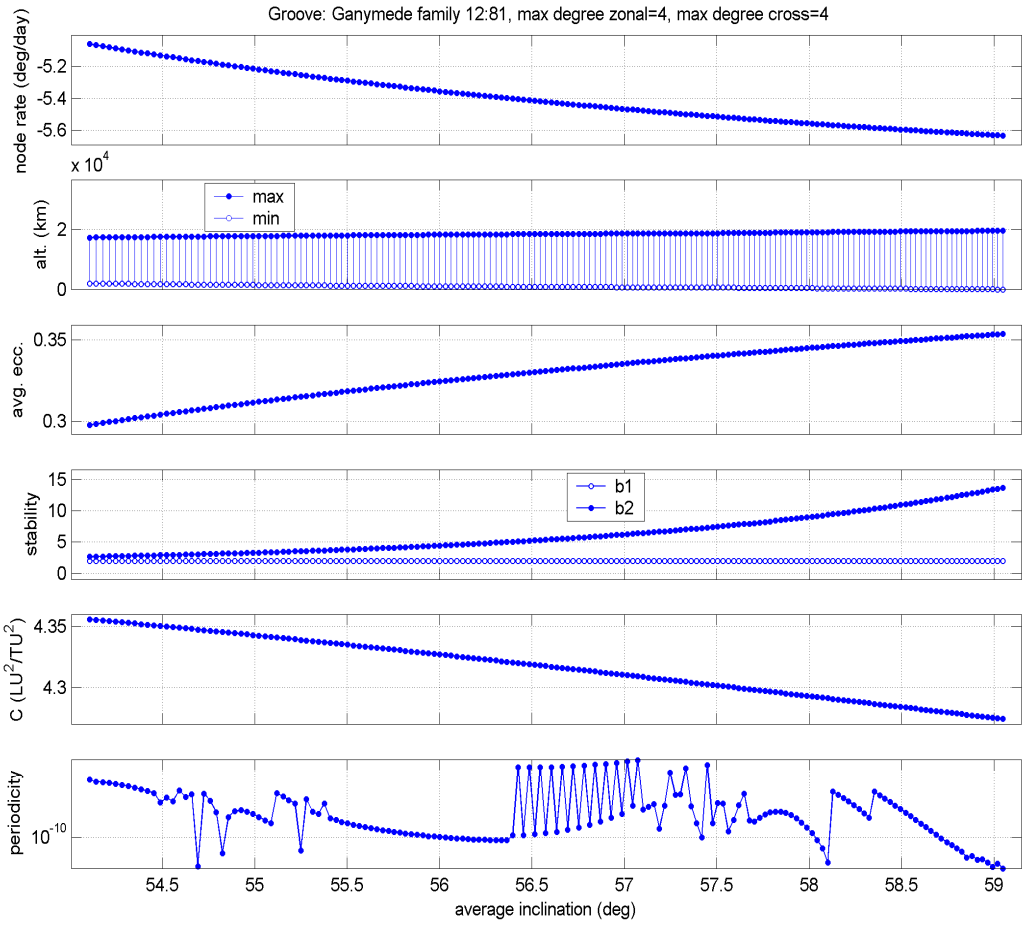

Figure 6: Promising family (12:81) of science orbits at Ganymede

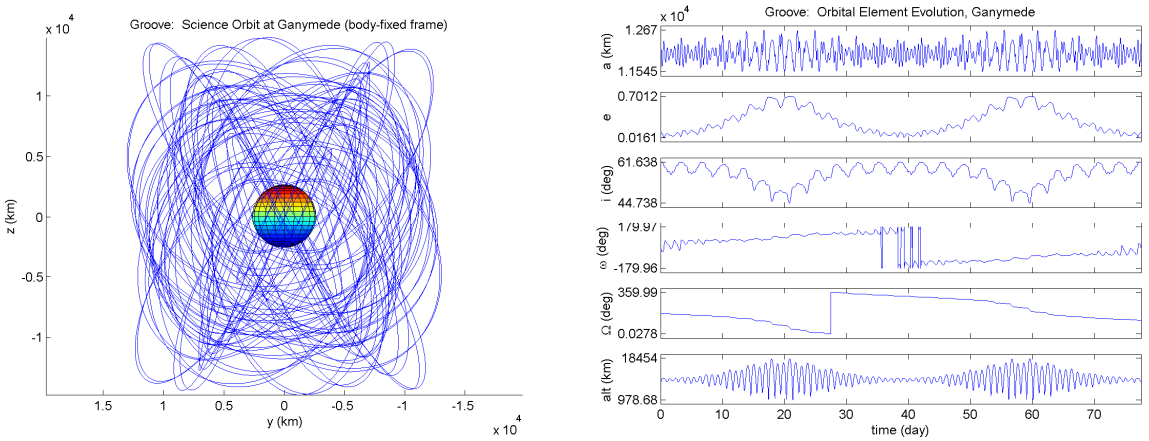

Figure 7: One period of example 12:81 science orbit: trajectory (left) and orbital elements (right)

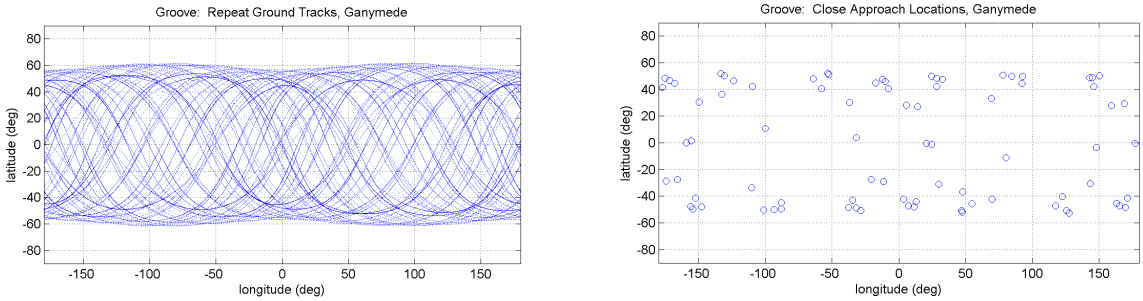

Figure 8: One period of example 12:81 science orbit: ground-tracks

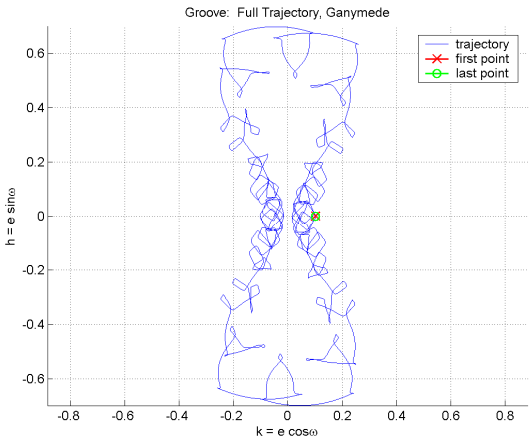

Figure 9: One period of example 12:81 science orbit: eccentricity vector repeat path

It is emphasized that the family shown in Figure 6 is simply one of several possible similar families. To illustrate, we also show a similar family of orbits with slightly lower periapses and larger periods (closer to the target 24 hours) in Figure 10. Note, contrary to the 12:81 family (although both families are very similar in nature), all of the orbits shown in Figure 6 of the 9:56 family are linearly stable as indicated by both stability indices being less than or equal to two. Therefore, in this model, the exact repeat orbits will remain intact over long propagations. An example 9:56 orbit is illustrated in Figure 11 - Figure 13. Note that the full cycle period of the 9:56 (~57 days) orbit is substantially less than that of the 12:81 (~78 days) orbit. This result is consistent with the the doubly averaged model where an increasing neck size of the figure-eight path corresponds with a smaller full cycle period (see Figure 9 and Figure 13).

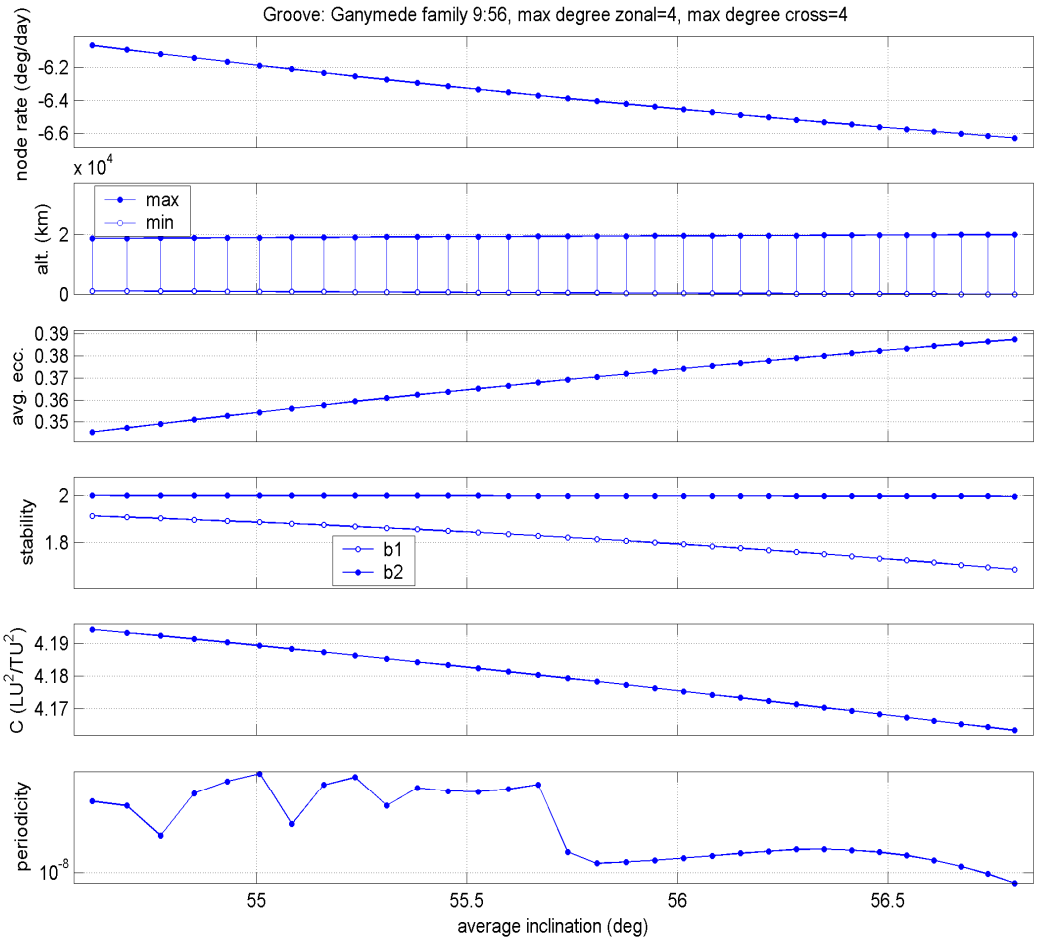

Figure 10: Promising family (9:56) of science orbits at Ganymede

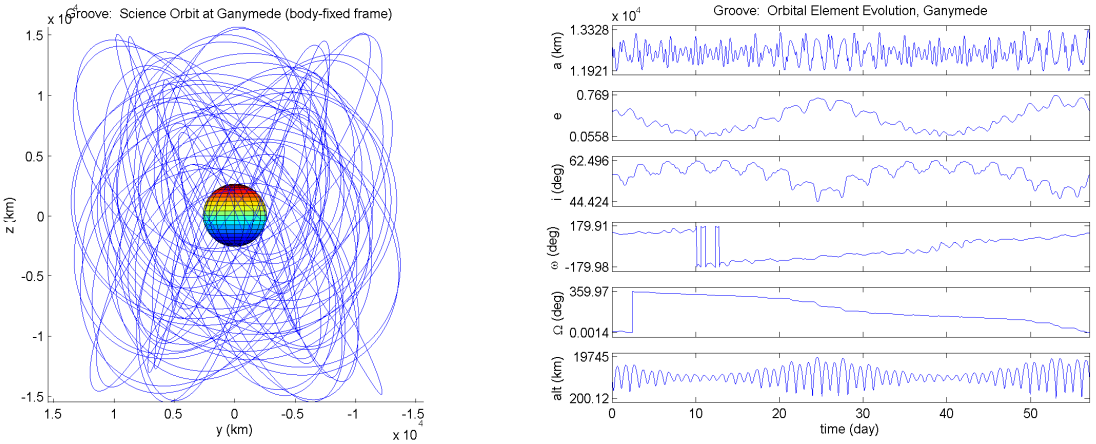

Figure 11: One period of example 9:56 science orbit: trajectory (left) and orbital elements (right)

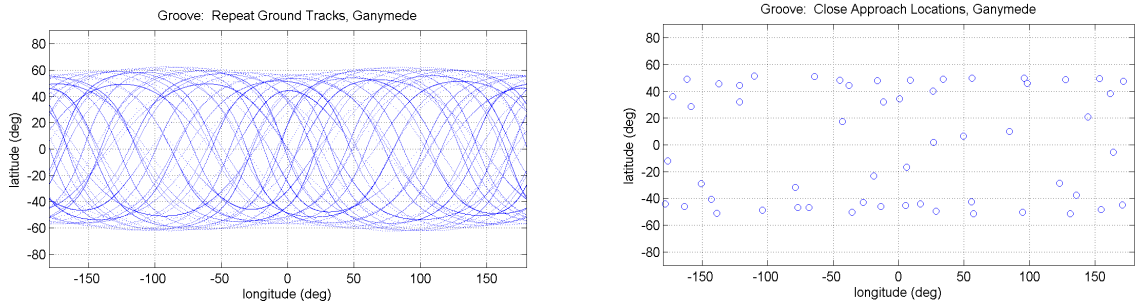

Figure 12: One period of example 9:56 science orbit: ground-tracks

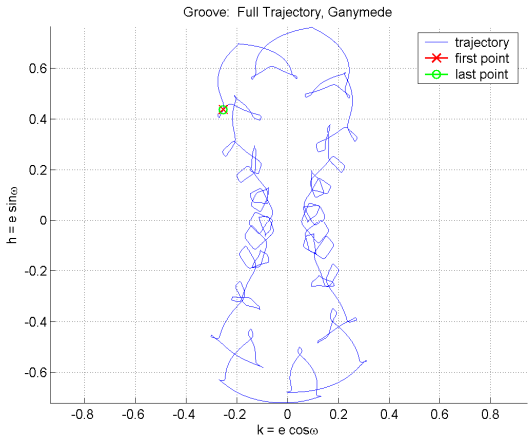

Figure 13: One period of example 9:56 science orbit: eccentricity vector repeat path

LONG-TERM N-BODY PROPAGATIONS

The important consideration of non-conservative perturbations (the realistic ephemeris for example) and force model uncertainties also play key roles in the detailed stability analysis and design of science orbits at planetary moons. While [5,6,11,14,15] represent progress in this area, more detailed analyses regarding the transition from simplified dynamics to ephemeris models is an important area of future research.

The stable solutions discussed in this study are considered linearly stable in the conservative force model including the Hill third-body perturbation and the non-spherical Ganymede gravity terms. The radius of the stability regions around the stable orbits in the presence of numerical and other perturbations is unclear. Methods using Fast Lyapynov Indicators (FLIs) are useful for estimating stability region radii [5,15]. While no such method has been applied in the current study, FLIs should be considered in future work. Further, the unstable orbits such as those of the 12:81 family may or may not be robust to realistic perturbations in terms of mission design. If the exact repeat pattern is destroyed yet the eccentricity keeps circulating with the same ranges, the instability is of little consequence. However, we have already demonstrated that the 24 hour orbit is likely pushing the boundaries of applicability for the doubly averaged dynamics, and further investigations are therefore necessary.

Ephemeris *n*-body propagations are a simple, crude approach to measuring stability radii or robustness of a particular solution to non-trivial perturbations. We proceed by propagating the two example orbits in ephemeris simulations involving two-body gravity from the Sun, Jupiter, Saturn, all the Galilean moons, and oblateness effects from Jupiter and Ganymede. By specifying the initial conditions given in Table 3 in the body-fixed frame at epoch, propagations beginning at arbitrary epochs have the effect of sampling uncertainties in the force model. If a particular orbit maintains its basic characteristics without impacting or escaping for one year starting at ten arbitrarily chosen epochs, it is considered long-term stable.

Figure 14 - Figure 16 show characteristics of the 9:56 example orbit ephemeris propagation. The epoch is arbitrarily chosen as Jan. 1, 2028 (Julian Date = 2461772.0). This orbit is deemed long-term stable as each of the ten different epochs led to orbital lifetimes of at least one year. By comparing the eccentricity vector path and the close approach locations of the simplified model equivalent orbit, it is clear that basic orbital characteristics are maintained during the long-term propagation. It should be noted that from Figure 11, the example orbit has a minimum altitude of ~200 km in the simplified model and Figure 16 shows consistency in the long-term ephemeris propagations. Because the orbits from family 12:81 are unstable in the simplified model, the example from Figure 7 is chosen with a higher minimum altitude of ~1000 km in anticipation of a less robust solution to the realistic perturbations. Although we do not explicitly illustrate the propagations, the 12:81 orbit also passes the long-term stability test for ten ephemeris propagations with arbitrary epochs. As predicted, however, the unstable 12:81 orbits lead to less repeatability in the ephemeris propagations and subsequently the minimum altitudes dip down to ~250 km as compared to the ~1000 km in the conservative model.

A brief analysis was performed to spot check the sensitivity of the long-term propagation to the non-spherical gravity of Ganymede. The same stability test of applying ten arbitrary epochs led to similar long-term stable results using only a Ganymede point mass. While this result is promising and certainly due to the large altitudes compared to the Ganymede radius, considerable future work is required to understand the non-spherical gravity-field implications.

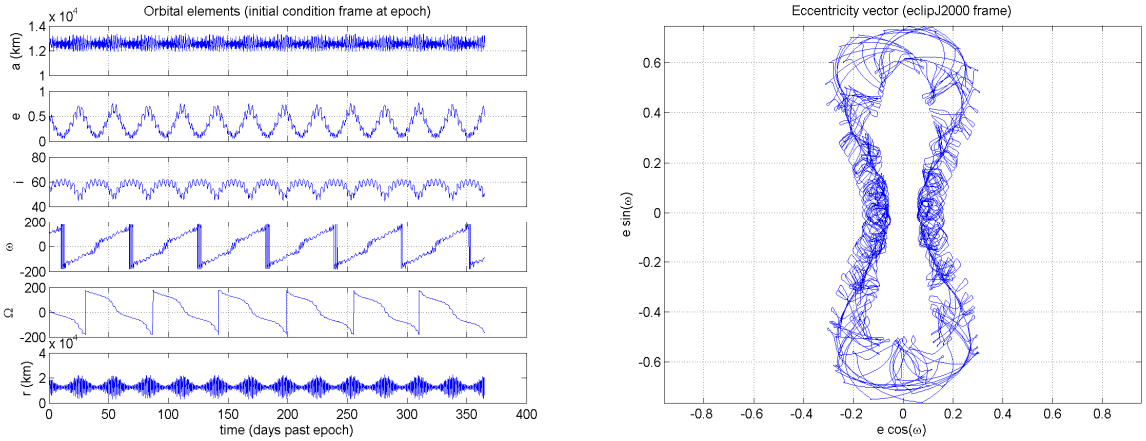

Figure 14: Long-term *n*-body ephemeris propagation for 9:56 orbit: orbital elements evolution (left) and eccentricity vector repeat path (right)

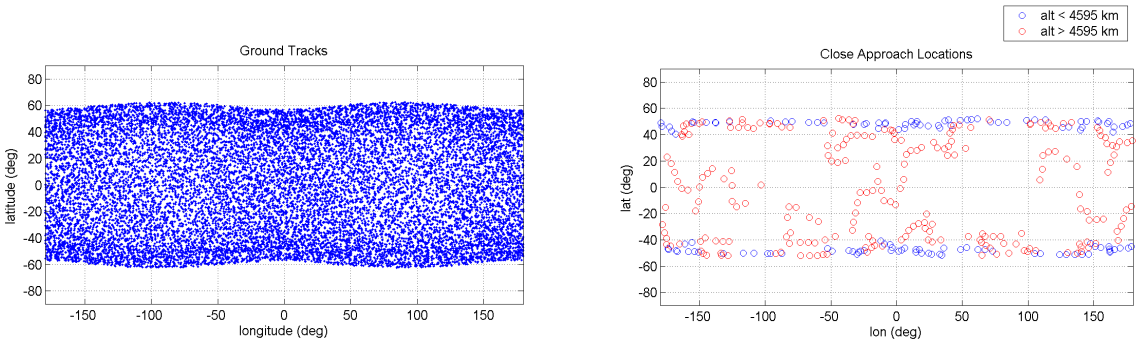

Figure 15: Long-term n-body ephemeris propagation for 9:56 orbit: Ground tracks

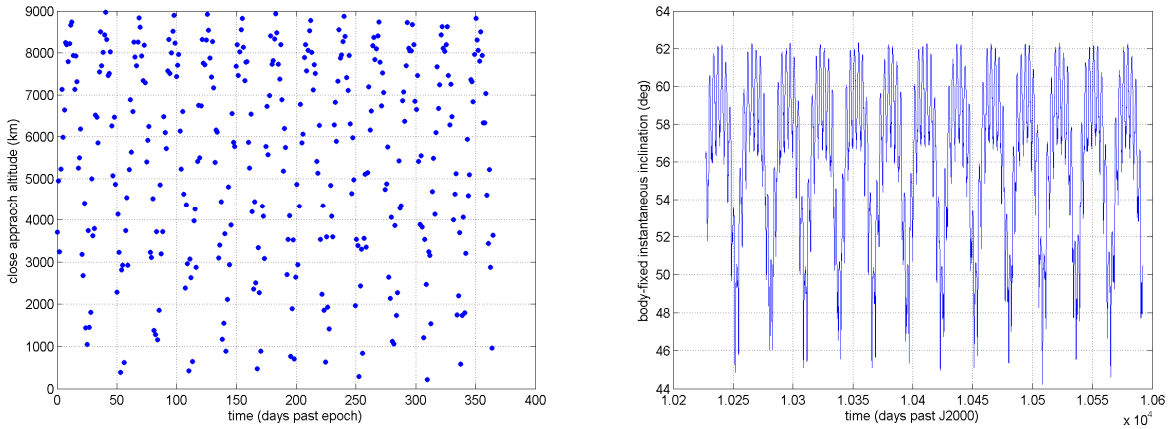

Figure 16: Long-term n-body ephemeris propagation for 9:56 orbit: close approach distances (left) and body-fixed *i* (right)

CONCLUSIONS

The first order effect of the third-body perturbation on a spacecraft near a planetary moon is reviewed, and a detailed contour plot analysis depicts all types of feasible motion. An emphasis is placed on eccentric orbits and mission design applications. In particular, the class of orbits that oscillate between near circular and highly eccentric and include a circulating argument of periapse is introduced as a viable, high-science value, low-cost trajectory design for planetary moon missions. These circulating figure-eight orbits are evaluated and documented in the context of maximizing sustainable inclinations for a variety of relevant moon systems. While the high eccentricity excursions occur at the lower bound of the inclination cycle, the orbits serendipitously spend the majority of their time at the higher inclinations. Quadrature expressions are derived for quick calculation of the full cycle periods.

While the doubly averaged system provides general insight to the third-body problem, we also rely on the periodic orbits in the un-averaged system for higher order solutions and validation of the doubly averaged predictions. As an example, two families of highly resonant periodic orbits are demonstrated in the un-averaged Hill plus 4x4 Ganymede gravity field model. Despite that the orbit period of ~24 hours is found to be just beyond the formal region of validity for the doubly averaged assumptions, the example orbits find general agreement with the doubly averaged predictions. The non-spherical gravity terms are found to have non-dominant effects on the high-altitude highly eccentric orbits. Finally, long-term ephemeris propagations are used to test the robustness of the example orbits to realistic perturbations. The example orbit from the 9:56 family is stable in the un-averaged model and finds best agreement when transitioning to the full ephemeris.

Considering all possible high altitude Ganymede orbits with occasional low-altitude close approaches, the proposed Ganymede science orbit enjoys inclinations that are likely at or near the maximum attainable for long-term stable motion. The orbit is circulating with close approaches distributed amongst all longitudes and $\pm 62^{o}$ latitude and it cycles between near-circular (9,000 km altitude) and highly eccentric (200 x 20,000 km altitude) approximately once a month. The high altitudes compared to the body-radius make both poles viewable at near-nadir pointing angles. The highly eccentric orbit is less expensive to achieve than a low-altitude circular orbit, and the orbital geometry and timing are favorable for Ganymede science as well as a variety of Jupiter system science.

In this study the circulating eccentric orbit is demonstrated in most detail for the Ganymede case. However, the general class of third body perturbed orbits is a cost-effective option for orbiting any modest sized planetary moon.

ACKNOWLEDGEMENTS

The authors thank Johnny Kwok, Nathan Strange, Jon Sims, Grace Tan-Wang, Tom Spilker, and David Senske for their interest and support of the project. Part of this work was carried out at the Jet Propulsion Laboratory, California Institute of Technology, under a contract with the National Aeronautics and Space Administration.

APPENDIX: GANYMEDE GRAVITY FIELD

Below are representative *normalized* gravity field coefficients for Ganymede originating from Galileo flyby data. The coefficients were used for the Jupiter Icy Moons Orbiter (JIMO) trajectory studies.

```
J(2)   =  5.911042930573900E-05,      C(3,3) = -7.575116779515599E-06,
J(3)   = -3.921720290616328E-07,      S(3,3) = -8.279091297771898E-07,
J(4)   =  1.619380392450006E-06,      C(4,1) =  4.018167872716952E-06,
C(2,1) = -1.089379888322607E-08,      S(4,1) =  5.830284294524415E-06,
S(2,1) = -1.204834981027450E-06,      C(4,2) = -9.205006749291541E-07,
C(2,2) =  6.152429561579210E-05,      S(4,2) = -7.719921073220343E-06,
S(2,2) = -5.410422638487023E-06,      C(4,3) =  1.807800500915109E-06,
C(3,1) = -6.863916460740865E-06,      S(4,3) =  3.883084011103666E-06,
S(3,1) = -5.971806445404929E-06,      C(4,4) =  3.101357600870122E-07,
C(3,2) = -6.481431518636326E-06,      S(4,4) =  5.656462546498310E-06
S(3,2) =  1.019584456216980E-05,
```

REFERENCES

[1] Aiello, J., "Numerical Investigation of Mapping Orbits about Jupiter's Icy Moons," paper AAS 2005-377, presented at the 2005 Astrodynamics Specialists Conference, Lake Tahoe, California, August 2005.

[2] Broucke, R., "Long-Term Third-Body Effects via Double Averaging," *Journal of Guidance, Control and Dynamics*, Vol. 26, No. 1, 2003, pp. 27–32.

[3] Johannesen, J.R., and D'Amario, L.A., "Europa Orbiter Mission Trajectory Design," paper AAS 99–360, presented at the 1999 AAS/AIAA Astrodynamics Specialist Conference, Girdwood, Alaska, August 1999.

[4] Lara, M., and San-Juan, J.F., "Dynamic Behavior of an Orbiter Around Europa," *Journal of Guidance, Control and Dynamics*, Vol. 28, No. 2, 2005, pp. 291–297.

[5] Lara, M., Russell, R., and Villac, B., "On Parking Solutions Around Europa" paper AAS 2005-384, presented at the 2005 AAS/AIAA Astrodynamics Specialist Conference, Lake Tahoe, California, August 2005.

[6] Lara, M., Russell, R.P., "On the Design of a Science Orbit about Europa," paper AAS 06-168, presented at the 16th AAS/AIAA Space Flight Mechanics Conference, Tampa, Florida, January 22-26, 2006.

[7] Lara, M., San-Juan, J.F., and Ferrer, S., "Secular Motion around TriAxial, Synchronously Orbiting, Planetary Satellites: Application to Europa," *Chaos: An Interdisciplinary Journal of Nonlinear Science*, Vol. 15, No. 4, 2005, pp. 1–13.

[8] Paskowitz, M.E. and Scheeres, D.J., "Orbit Mechanics about Planetary Satellites," paper AAS 04-244, presented at the Space Flight Mechanics Meeting, Maui, Hawaii, February 2004.

[9] Paskowitz, M.E., and Scheeres, D.J., "Transient Behavior of Planetary Satellites Including Higher Order Gravity Fields," paper AAS 2005-358, presented at the 2005 Astrodynamics Specialists Conference, Lake Tahoe, California, August 2005.

[10] Scheeres, D.J., Guman, M.D., and Villac, B.F., "Stability Analysis of Planetary Satellite Orbiters: Application to the Europa Orbiter," *Journal of Guidance, Control, and Dynamics*, Vol. 24, No. 4, 2001, pp. 778–787.

[11] Lara, M., Russell, R. P., "On the Computation of a Science Orbit about Europa," *Journal of Guidance, Control, and Dynamics*. Vol. 30, No. 1, 2007, pp. 259-263.

[12] Lara, M., Russell, R.P., Villac, B. "Classification of the Distant Stability Regions at Europa," *Journal of Guidance, Control, and Dynamics*, Vol. 30, No. 2, 2007, pp. 409-418.

[13] Russell, R. P., "Global Search for Planar and Three-dimensional Periodic Orbits Near Europa," *Journal of the Astronautical Sciences*. Vol. 54, No. 2, 2006, pp. 199-226.

[14] Russell, R. P., Lara, M., "Long-Life Lunar Repeat Ground Track Orbits," *Journal of Guidance, Control, and Dynamics*, Vol. 30, No. 4, 2007, pp. 982-993.

[15] Lara, M., Russell, R.P., Villac, B. "Fast estimation of stable regions in real models," *Meccanica*, DOI 10.1007/s11012-007-9060-z.

[16] Lara, M., "Searching for Repeating Ground Track Orbits: A Systematic Approach," *Journal of the Astronautical Sciences*, Vol. 47, 1999, pp. 177–188.

[17] Lara, M., "Repeat Ground Track Orbits of the Earth Tesseral Problem as Bifurcations of the Equatorial Family of Periodic Orbits," *Celestial Mechanics and Dynamical Astronomy*, Vol. 86, No. 2, 2003, pp 143-162.

[18] Ely, T., "Stable Constellations of Frozen Elliptical Inclined Lunar Orbits," *Journal of the Astronautical Sciences*, Vol. 53, No. 3, 2005, pp. 301-316.

[19] Russell, R.P. "Enceladus Science Orbit Design," Jet Propulsion Laboratory Interoffice Memo, 343M-2007-04, July 2007.

[20] Tapley, B.D., Schutz, B.E., Born, G.H., *Statistical Orbit Determination*, Elsevier Academic Press, Burlington, MA, 2004. Sec. 2.3.

[21] Battin, R. H., *An Introduction to the Mathematics and Methods of Astrodynamics*, American Institute of Aeronautics and Astronautics, New York, 1987, pg. 483.

[22] Seidelmann, P.K., Abalakin, V.K., Bursa, M., Davies, M.E., Bergh, C. de, Lieske, J.H., Oberst, J., Simon, J.L., Standish, E.M., Stooke, P., Thomas, P.C., "Report of the IAU/IAG Working Group on Cartographic Coordinates and Rotational Elements of the Planets and Satellites: 2000," *Celestial Mechanics and Dynamical Astronomy*, Vol. 82, Issue 1, 2002, pp. 83–111.

[23] Kwok, J. H., "Long-Term Orbit Prediction Using an Averaging Method," AIAA Paper 84-1985, Aug. 1985.

[24] Kwok, J. H., "DoublyAveragingMethod forThird Body Perturbations," American Astronautical Society, Paper 91-464, Aug. 1991.

[25] Russell, R. P., "Global Search for Planar and Three-dimensional Periodic Orbits Near Europa," Journal of the Astronautical Sciences. Vol. 54, No. 2, 2006, pp. 199-226.

[26] Henon, M. "Numerical Exploration of the Restricted Problem. V. Hill's Case: Periodic Orbits and Their Stability," Astronomy and Astrophysics, Vol. 1, 1969, pp. 223–238.